2010

Mesoporous Tin Oxide as an Oxidation-Resistant Catalyst Support for Proton Exchange Membrane Fuel Cells

Peng Zhang
University of South Carolina - Columbia

Sheng-Yang Huang
University of South Carolina - Columbia

Branko N. Popov
university of south, popov@engr.sc.edu

Publication Info

Journal of the Electrochemical Society, 2010, pages B1163-B1172.

Publisher's link: http://dx.doi.org/10.1149/1.3442371
DOI: 10.1149/1.3442371

Journal of The Electrochemical Society, **157** (8) B1163-B1172 (2010)
0013-4651/2010/157(8)/B1163/10/$28.00 © The Electrochemical Society

Mesoporous Tin Oxide as an Oxidation-Resistant Catalyst Support for Proton Exchange Membrane Fuel Cells

Peng Zhang, Sheng-Yang Huang, and Branko N. Popov[*,z]

Center for Electrochemical Engineering, Department of Chemical Engineering, University of South Carolina, Columbia, South Carolina 29208, USA

Mesoporous catalyst support based on tin oxide (SnO_2) is synthesized with high surface area of 205 m^2 g^{-1} and with narrow pore size distribution. Modified polyol method is used to deposit platinum on SnO_2. The physical properties of the support and the SnO_2-supported Pt catalyst (Pt/SnO_2) are characterized by using the Brunauer, Emmett, and Teller method, X-ray diffraction, and transmission electron microscopy. The electrochemical stability and durability of the Pt/SnO_2 catalyst are investigated by the accelerated stress tests proposed by the U.S. Department of Energy. Pt/SnO_2 catalyst exhibits electrochemical activity in fuel cells comparable to that of Pt/C. More importantly, the electrochemical stability of the Pt/SnO_2 catalyst significantly improves when compared with the commercial Pt/C catalyst at high potentials (~1.2 V vs reversible hydrogen electrode).
 [DOI: 10.1149/1.3442371]

Manuscript submitted January 11, 2010; revised manuscript received May 7, 2010. Published June 8, 2010.

The performance and stability of proton exchange membrane fuel cells (PEMFCs) is mainly controlled by platinum-particle dissolution and sintering,[1-4] carbon support corrosion, and membrane thinning. Carbon due to its large surface area, high electrical conductivity, and well-developed pore structure is commonly used as a catalyst support material for PEMFCs.[5-8] However, porous carbon support is susceptible to corrosion at the cathode interface under PEMFC operating conditions such as high water content, low pH, and high temperature from 50 to 90°C. Furthermore, Reiser et al.[9] reported that when the anode is partially exposed to hydrogen and partially exposed to oxygen during start–stop procedures, this causes flow of current opposite to the normal fuel cell mode at the oxygen-exposed region and raises the cathode interfacial potential difference to 1.44 V, which, in the presence of Pt nanoparticles, results in a cathode severe corrosion through the following reaction[10]

$$C + 2H_2O \rightarrow CO_2 + 4H^+ + 4e^-(0.207\ V\ vs\ RHE,\ 25°C) \quad [1]$$

where RHE is reference hydrogen electrode.

Carbon oxidation results in the hydrophilic effects that prevent water removal and thus leads to increased mass-transport losses and decreased thickness of the catalyst layer, which increases the cell resistance. Carbon corrosion also leads to electrically isolated Pt particles that are detached from the support. These factors finally cause a rapid degradation in the Pt catalysts in PEMFCs. Jarvi et al.[11] investigated the platinum catalyzed effect on corrosion of carbon supports with various Pt mass fractions under PEMFC conditions. Carbon-only (or Pt-free) electrodes in membrane electrode assembly (MEA) had low CO_2 emission at high potentials, whereas the CO_2 emission rates were much higher in the presence of Pt. In addition, the CO_2 generation rates increased with higher Pt mass fraction in the electrodes.[12-15]

It is desirable to use more robust noncarbon materials such as metal oxides as catalyst supports in PEMFCs. A variety of conducting oxides with highly oxidation-resistant properties such as titanium oxides,[16] niobium oxides,[17] niobium-doped titanium oxides,[18] indium tin oxides (ITO),[19] iridium oxides,[20] antimony-doped tin oxides,[21] and tungsten oxides[22] have been studied as potential catalyst-support candidates. Even though improved stability in PEMFC performance was achieved using these metal oxides, the low electrical conductivity and the surface area resulted in the poor dispersion of Pt on the supports, leading to low electrochemical activity. In this paper, tin oxide (SnO_2) was prepared as a catalyst support due to its unique electrical, chemical, and physical properties.

* Electrochemical Society Active Member.
[z] E-mail: popov@cec.sc.edu

Experimental

Synthesis of mesoporous SnO_2.— Mesoporous SnO_2 was synthesized via a neutral-surfactant template-assisted method.[23] A typical synthesis procedure is as follows: A tin(IV) chloride sol solution was prepared by mixing a measured amount of $SnCl_4$ with deionized water. The pH value of the sol solution was adjusted to 7–8 by the addition of ammonium hydroxide (25%). A calculated amount of tetraethyl orthosilicate (TEOS) was added to the sol solution and stirred for 30 min. Next, a tetradecylamine solution was carefully added to the $SnCl_4$/TEOS mixture. The final solution was held at room temperature for 24 h, followed by another 24 h of aging at 75°C. The white precipitated product was washed and filtered using deionized water at least three times. The resulting white powder was dried at 80°C overnight. After etching the silica template with NaOH solution, the as-prepared powder was finally calcined at 400°C for 3–6 h.

Preparation of Pt/SnO_2.— Synthesis of Pt/SnO_2 catalysts was based on the polyol method.[24] The desired amount of H_2PtCl_6 was dissolved in 200 mL of ethylene glycol. 0.2 M NaOH was used to adjust the pH of the solution to 12, and then the solution was refluxed at 160°C for 3 h in an inert atmosphere to ensure the complete reduction of $[PtCl_6]^{2-}$ to platinum. The resultant Pt colloid was mixed with an aqueous solution of SnO_2 nanoparticles. After stirring for several hours, 1 M H_2SO_4 was added to decrease the pH of the solution to 3. The final mixture was washed with a large amount of hot water and filtered. The collected product was dried at 80°C overnight before further characterization studies.

To compare the electrochemical activity and stability of the laboratory-synthesized and commercial catalysts, a 45.9 wt % Pt/C catalyst (TEC10E50E) was obtained from Tanaka Kikinzoku Kogyo K.K. and platinum black (HiSPEC 1000) was purchased from Alfa Aesar.

Material characterizations.— The physical properties of the SnO_2 support and Pt/SnO_2 catalysts were characterized by the Brunauer, Emmett, and Teller method (BET) (Quantachrome Instrument), X-ray diffraction (XRD), and transmission electron microscopy (TEM). XRD analysis was performed using a Rigaku X-ray diffractometer in a 2θ range 20–90° with Cu Kα radiation. A tube voltage of 30 kV and a current of 15 mA were used during the scanning. TEM was carried out using a JEOL-2100F microscope equipped with a field-emission electron gun source operated at 200 kV.

RRDE and CV measurements.— Electrochemical characterizations were performed in 0.5 M H_2SO_4 using a Pine bipotentiostat (model AFCBP1), Pt wire counter electrode, and Hg/Hg_2SO_4 reference electrode of 0.68 V vs RHE. The rotating ring-disk electrode (RRDE) with a Pt ring and a glassy carbon disk (0.247 cm^2) was

used as the working electrode. The catalyst ink was prepared by blending the catalyst powder with ethanol in an ultrasonic bath. The required amount of the catalyst ink was deposited onto the glassy carbon disk using a micropipette. 5 μL of Nafion solution (0.25 wt % Nafion) was added on top of the catalyst layer to minimize anion adsorption effects on the catalysts.[25]

The electrolyte was purged with nitrogen (99.999%), and cyclic voltammograms (CVs) were recorded before the O_2 reduction measurements. The CV was recorded in aqueous electrolyte purged with nitrogen to obtain the background capacitive currents and electrochemical surface area (ECSA) of the Pt. The ECSA of the Pt was determined by charge integration under the hydrogen desorption peaks, assuming a charge of 210 $\mu C\ cm^{-2}$ for the electroactive Pt surface. The electrolyte was purged with oxygen (99.999%) for 30 min before measurement. The linear sweep voltammograms were recorded at different rotation speeds of the RRDE. The oxygen reduction current was calculated from the difference between currents measured in the nitrogen- and oxygen-saturated electrolytes.

PEMFC performance.— The cathode catalyst ink was prepared by ultrasonically blending the catalyst powder with Nafion solution (5 wt %) and ethanol for 4 h. The catalyst ink was then spray-coated onto a gas diffusion layer (GDL, ELAT LT1400W, BASF). The weight ratio of Pt catalyst to Nafion was kept at 4:1. Commercially available catalyzed GDL (LT140EW low temperature ELAT GDE microporous layer, BASF) was used as the anode for all fuel cell experiments. The anode catalyst loading was 0.5 mg Pt cm^{-2}. The fuel cell tests were carried out in a single cell with an electrode area of 5 cm^2. H_2 gas (99.999%) humidified at 77°C [relative humidity (RH) 100%] and O_2 gas (99.999%) humidified at 75°C (RH 100%) were supplied to the anode and cathode compartments, respectively, each at a flow rate of 150 mL min^{-1}. Polarization experiments were conducted using a fully automated test station (Fuel Cell Technologies Inc.) at 75°C.

Accelerated stress tests.— The electrochemical durability and stability of the Pt/C and Pt/SnO_2 cathode catalysts were examined using accelerated stress test protocols (ASTP) suggested by U.S. DOE.[26] The tests were carried out in a single cell with an electrode area of 25 cm^2. In ASTP I, the catalyst support durability of both types of catalysts was compared by holding the cell potential at 1.2 V with the anode and cathode exposed to hydrogen and nitrogen, respectively. To further characterize the catalyst support properties, polarization curves and full-scale CVs (50 mV s^{-1}) recorded over the voltage range from 0 to 1.2 V were measured every 24 h. As suggested in ASTP II, continuous potential cycling between 0.7 and 1.2 V at 50 mV s^{-1} at various temperatures with periodic measurements of polarization curve and ECSA was performed to determine the electrochemical stability of the Pt/C and Pt/SnO_2 catalysts. TEM and electrochemical impedance spectra were used to measure the Pt particle size and resistance in the MEAs before and after the ASTP II tests.

Results and Discussion

Structural characterization.— The synthesized SnO_2 nanoparticles and the Pt/SnO_2 catalyst were analyzed by XRD. The bottom diffractogram in Fig. 1 shows the typical polycrystalline diffraction of cassiterite SnO_2, as indicated by three predominant peaks from the (110), (101), and (211) planes. The size of the SnO_2 nanoparticles was calculated from the (110) peak using Scherrer's equation at ~6.1 nm. The Pt/SnO_2 catalyst exhibited a characteristic pattern of polycrystalline Pt diffraction. The diffraction peaks at approximately 39, 46, 68, and 80° are due to diffractions at the Pt(111), (200), (220), and (311) planes, respectively. The Pt particle size calculated from the (111) peak using Scherrer's equation was ~5.2 nm. For the Pt/C, the patterns of the Pt characteristic peaks were too broad to be resolved, indicating very small Pt particles (~2.5 nm confirmed by the TEM image, as shown in Fig. 18a).

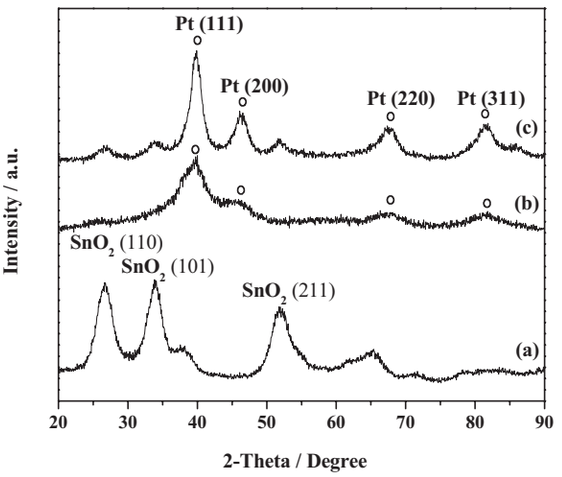

Figure 1. XRD patterns of (a) SnO_2 support, (b) Pt/C, and (c) Pt/SnO_2 catalysts.

The details of the BET analysis for surface area, pore size, and pore volume are summarized in Table I. The SnO_2 nanoparticles showed a high BET surface area of 205 $m^2\ g^{-1}$ and an average pore diameter of 13.4 nm, indicating the presence of a mesoporous framework. When Pt was deposited on the SnO_2 support, the values of the BET specific surface area, pore size, and pore volume of the Pt/SnO_2 catalyst decreased compared to those of pure SnO_2. This is because the Pt nanoparticles were dispersed within the pores of the porous SnO_2 support, leading to blocking of the pore channels and a consequent decrease in the measured surface area, pore size, and pore volume.[27]

The nitrogen sorption (adsorption and desorption) isotherms and their corresponding Barrett–Joyner–Halenda (BJH) pore size distributions for SnO_2 and Pt/SnO_2 are shown in Fig. 2 and 3, respectively. The SnO_2 isotherms showed large hysteresis loops at high relative pressures. The adsorption/desorption pattern matches a type-IV behavior for mesoporous adsorbents with strong affinities. This fact was further confirmed by the pore size distribution curves showing pore sizes centered at 13.4 nm.

Electrochemical characterizations.— The electrochemical properties of SnO_2 and the commercial carbon supports (Ketjen Black EC-300J and Vulcan XC-72) were examined using CV. Figure 4 shows CV curves for SnO_2, Ketjen Black EC-300J, and Vulcan XC-72 obtained at a scan rate of 50 mV s^{-1} in 0.5 M H_2SO_4. The potential was scanned from 0 to 1.3 V vs RHE. In the positive direction sweep, below 0.9 V, only the double-layer charging current was observed for all three supports. At potentials above 0.9 V, the anodic current for Ketjen Black EC-300J and Vulcan XC-72 carbon increased with the increase in the potentials, whereas only a small anodic current was observed for the SnO_2 support up to 1.3 V, suggesting its high resistance toward oxidation when subjected to high positive potentials, indicating its high resistance toward oxidation when subjected to high positive potentials.

To evaluate the electrochemical activity of the Pt/SnO_2 catalyst, the oxygen reduction reaction (ORR) was studied using RRDE with

Table I. Results of the BET analysis.

Sample	BET surface area ($m^2\ g^{-1}$)	BJH pore size (nm)	BJH pore volume ($mL\ g^{-1}$)
Vulcan XC-72	230	5.9	0.339
SnO_2	205	13.4	0.346
Pt/SnO_2	102	6.6	0.197

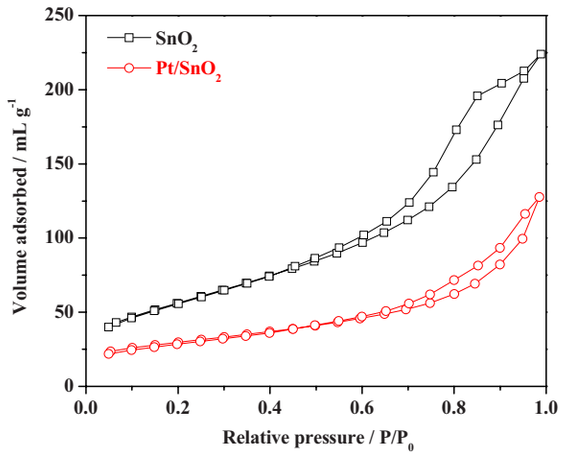

Figure 2. (Color online) N_2 adsorption isotherms of the SnO_2 support and the Pt/SnO_2 catalyst.

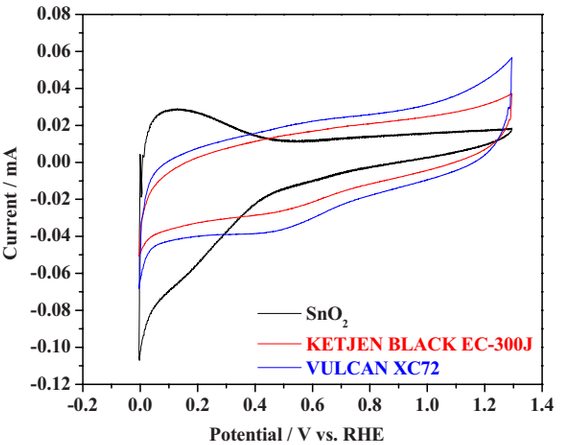

Figure 4. (Color online) CVs of the SnO_2, Ketjen Black EC-300J, and Vulcan XC-72 carbon obtained at a scan rate of 50 mV s^{-1} in 0.5 M H_2SO_4.

different Pt loadings (60, 80, 100, and 120 μg cm^{-2}) on the glassy carbon electrode. Figure 5 shows the polarization curves for ORR with the Pt/SnO_2 catalyst. The polarization curve of pure SnO_2 indicated that SnO_2 was electrochemically inert to the oxygen reduction and showed negligible current. At high potentials, the ORR is under the kinetic-diffusion control region, followed by a purely diffusion-limited region between 0.55 and 0.1 V vs RHE. The limiting currents increased with the increase in Pt loading levels on the glassy carbon electrode.

Figure 6a shows the compared polarization curves for ORR on Pt/SnO_2, Pt black, and Pt/C, each with the same amount of Pt loading. The limiting current of Pt/SnO_2, which was similar to that of Pt/C, was much higher than that of Pt black. Figure 6b depicts the mass activities for all three Pt catalysts, obtained from the kinetic currents divided by the Pt mass at 0.85 V. The mass activity of Pt/SnO_2 was slightly higher than that of the Pt black catalyst. The improved activity of Pt/SnO_2 may be attributed to the good dispersion of Pt nanoparticles on the nanosized SnO_2 support. In addition to the dispersion effect on the catalyst, an interaction between the SnO_2 support material and the Pt metal may have led to an excellent activity for the Pt/SnO_2 catalyst for oxygen reduction.

The mechanism of the overall ORR is assumed to consist of four separate single-electron transfer steps. A linear Tafel plot is expected for this four-electron reaction mechanism when the potential is lower than the standard electrode potential of 1.229 V vs RHE. The potential region of 1.0–0.6 V is the practical range of PEMFC application. Figure 7 shows the Tafel plots derived from the kinetic currents, j_k of the three Pt catalysts. The Tafel slope for the Pt/SnO_2 catalyst was −104 mV dec^{-1} above 0.80 V, while that for the commercial Pt black and Pt/C were −98 and −105 mV dec^{-1}, respectively, in the same potential range. The intrinsic Tafel slope in acid solution has been reported as −118 mV dec^{-1} in the absence of adsorbed anions. The lower values of the slope were due to the blocking and/or electronic effects of the adsorbed species.[28] The Tafel slopes obtained from the Pt/SnO_2 catalyst suggested that OH adsorption may have little effect on the Pt surfaces on SnO_2 oxides within the observed potential range (0.8–0.9 V).[22]

Figure 8 shows the polarization curves for the ORR with the Pt/SnO_2 catalyst at various rotation speeds (100–1700 rpm) at a scan rate of 5 mV s^{-1}. The considerable activity of the catalysts was indicated by the high onset potential for O_2 reduction (0.95–1.0 V) as well as by the high half-wave potentials. The shapes of the voltammograms of Pt/SnO_2 showed very well-defined mass-transfer and kinetic regions similar to those obtained for oxygen reduction on conventional Pt/C catalysts. The ORR was under mixed kinetic-diffusion control in the high potential region, followed by the region where the diffusion-limiting currents were observed. Single-step reduction waves with well-developed limiting-current plateaus were observed at all rotation speeds. Furthermore, the low peroxide for-

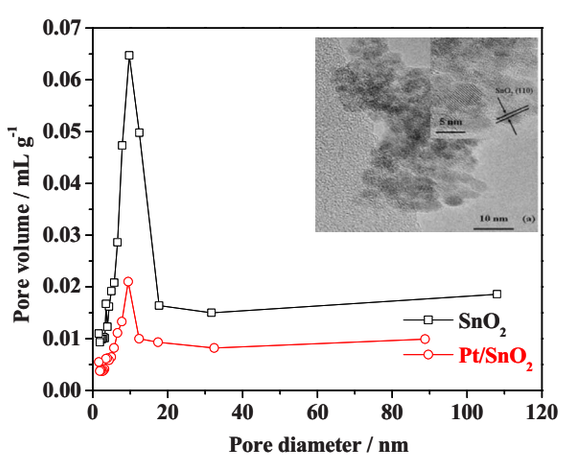

Figure 3. (Color online) BJH pore size distribution of the SnO_2 support and the Pt/SnO_2 catalyst (inset: the TEM image of pure SnO_2 support).

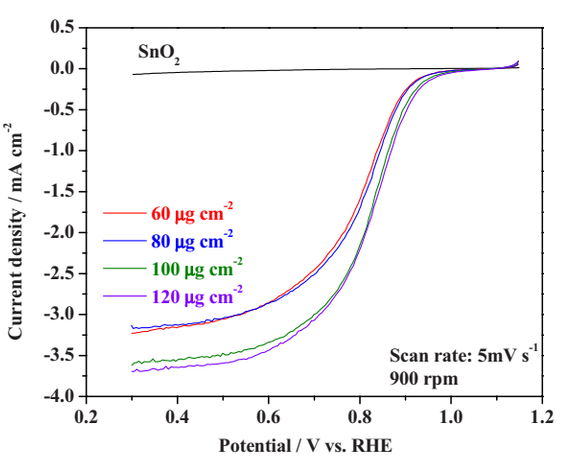

Figure 5. (Color online) Linear sweep voltammograms of the SnO_2 and the Pt/SnO_2 catalyst for the ORR with various Pt loadings.

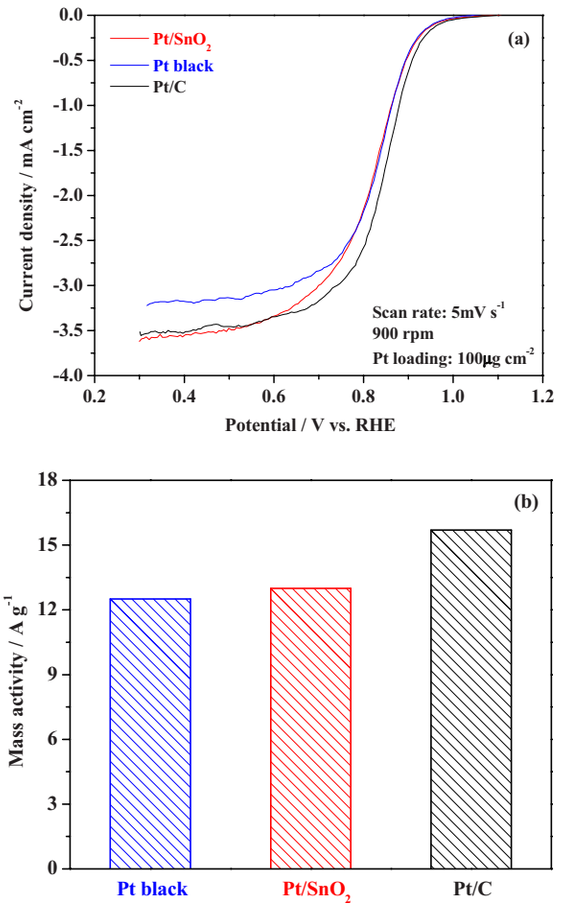

Figure 6. (Color online) (a) Linear sweep voltammograms and (b) mass activity at 0.85 V of the Pt/SnO_2, Pt black, and Pt/C catalysts for the ORR.

mation (<2%, not shown here) implied that the Pt/SnO_2 catalyst was highly selective for the ORR via the four-electron process.[29]

The stability from CV measurement.— The durability of the Pt/SnO_2 catalyst was characterized for up to 1600 cycles in a N_2-saturated 0.5 M H_2SO_4 solution at room temperature by voltage

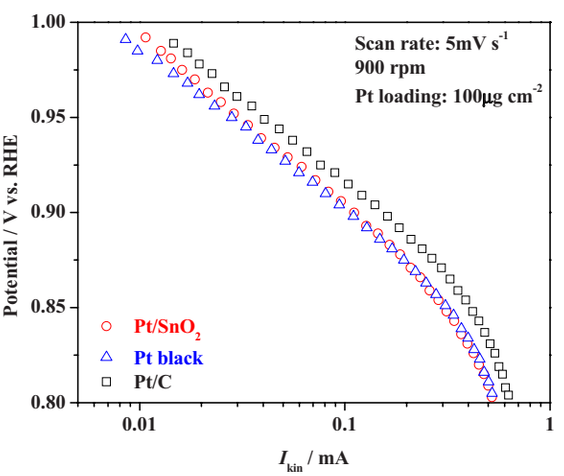

Figure 7. (Color online) Tafel slopes derived from the kinetic currents for the Pt/SnO_2, Pt black, and Pt/C catalysts.

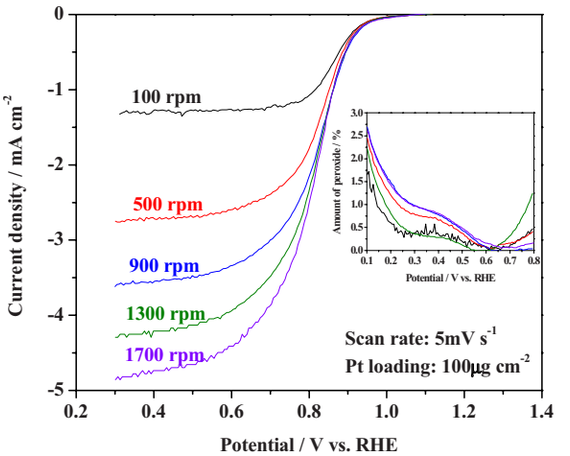

Figure 8. (Color online) Linear sweep voltammograms of the Pt/SnO_2 catalyst for the ORR at various rotation speeds (inset: Amount of H_2O_2 produced on Pt/SnO_2 for ORR).

cycling at higher potentials and compared with the Pt/C catalyst. A considerable corrosion of carbon supports, associated with a decrease in the catalyst layer thickness due to carbon electro-oxidation and with aggregation and growth of Pt nanoparticles at high potentials approaching 1.3 V, has been reported.[30,31] The intensity of the

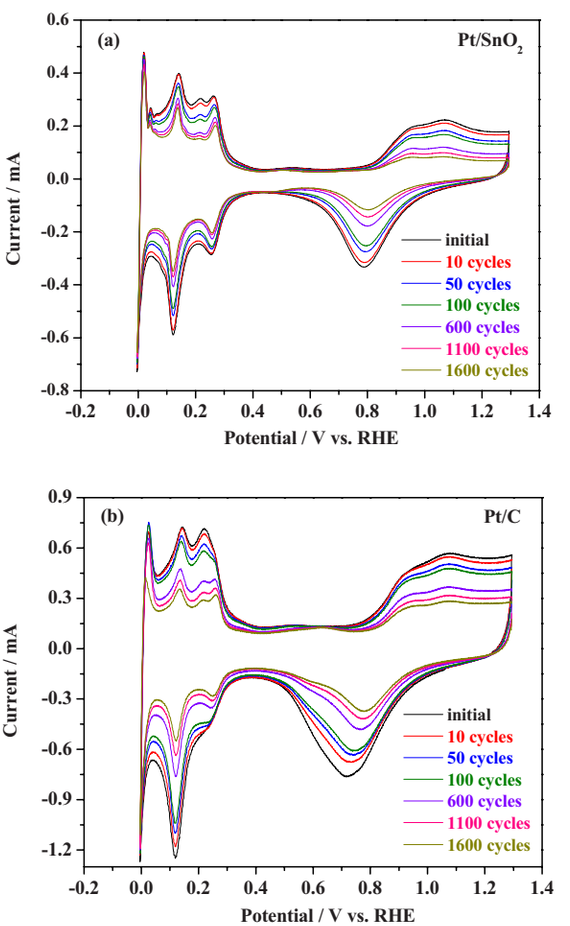

Figure 9. (Color online) CVs of (a) Pt/SnO_2 and (b) Pt/C at a scan rate of 50 mV s^{-1} in 0.5 M H_2SO_4.

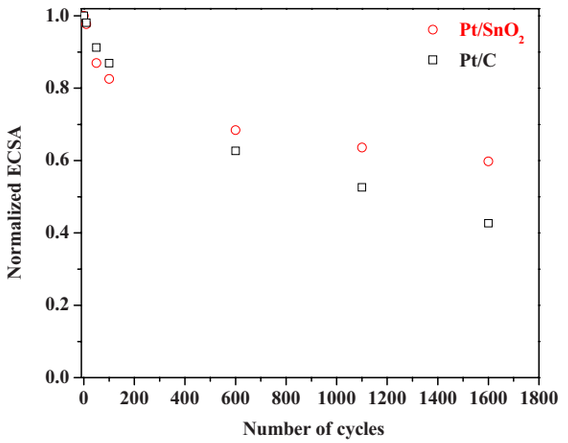

Figure 10. (Color online) Normalized ECSA as a function of the number of CV cycles for the $PtSnO_2$ and Pt/C catalysts.

hydrogen adsorption/desorption peaks in the CVs of Pt/C shown in Fig. 9b changed significantly, whereas those of the Pt/SnO_2 CVs (shown in Fig. 9a) were unchanged. Pt/C peak positions shifted dramatically as the surface area was reduced by 40% over 600 cycles, while the Pt/SnO_2 CV shapes again remained nearly unchanged. The electrochemically active surface area, however, was reduced by only 20% after 1600 cycles. Similar results were observed by other researchers when ITO was used as a catalyst support.[19] A 40 wt % Pt supported on Vulcan carbon suffered a loss of almost all of its active area after only 50 cycles during potential cycling from 0.6 to 1.8 V, whereas the Pt reduction peak for Pt/ITO did not shift even after 100 cycles at the same potential cycling range.[19] Evidence has also been presented that tin oxide supports could bear even more severe oxidation conditions (up to 1.5 V).[32]

Figure 10 shows the normalized ECSA as a function of the cumulative number of potential cycles for the Pt/SnO_2 and Pt/C catalysts. Both samples exhibited a gradual decline in surface area with successive potential cycling, probably due to Pt dissolution or migration and growth of Pt particles on/off the supports.[3] The total surface area loss in the Pt/C sample was about 60%. The surface area losses were 40% for the Pt/SnO_2 catalyst, which indicated that the Pt/SnO_2 catalyst was much more electrochemically stable than the Pt/C catalyst. The smaller surface area loss for the Pt/SnO_2 catalyst during potential cycling test could be attributed to the relatively high corrosion resistance of the SnO_2 support. The greater

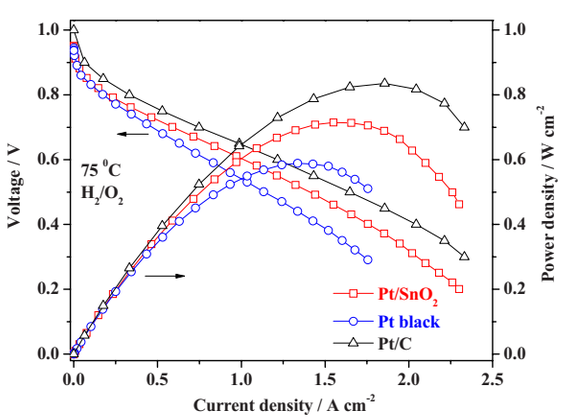

Figure 11. (Color online) Polarization curves of the PEMFCs with the Pt/SnO_2, Pt black, and Pt/C catalysts.

Table II. ASTP I.

Catalyst support cycle	
Cycle	Hold at 1.2 V for 24 h
Total time	Continuous operation for 200 h
Temperature	80°C
RH	Anode/cathode 100/100%
Fuel/oxidant	Hydrogen/nitrogen
Pressure	150 kPa absolute

corrosion resistance of SnO_2 over commercial carbon supports in an acid environment was demonstrated by CV, as previously shown in Fig. 4.

Fuel cell initial performance.— Each single cell of 5 cm^2 MEA was operated on ambient pressure of saturated hydrogen/oxygen until performance had stabilized. Figure 11 shows the polarization curves of PEMFCs using Pt/SnO_2, Pt black, and Pt/C as cathode catalysts. In this figure, the current densities at 0.7 V reached to 0.61, 0.48, and 0.72 A cm^{-2} with maximum power densities of 0.74, 0.58, and 0.81 W cm^{-2} for the Pt/SnO_2, Pt black, and Pt/C catalysts, respectively. The fuel cell performance of the Pt/SnO_2 was comparable to that of the Pt/C catalyst. This may be due to the difference in thickness of the cathode catalyst layers. At the targeted Pt loading, the thickness of the catalyst layer with Pt/C was ~10 μm, whereas an ultrathin catalyst layer (~1 μm) was ob-

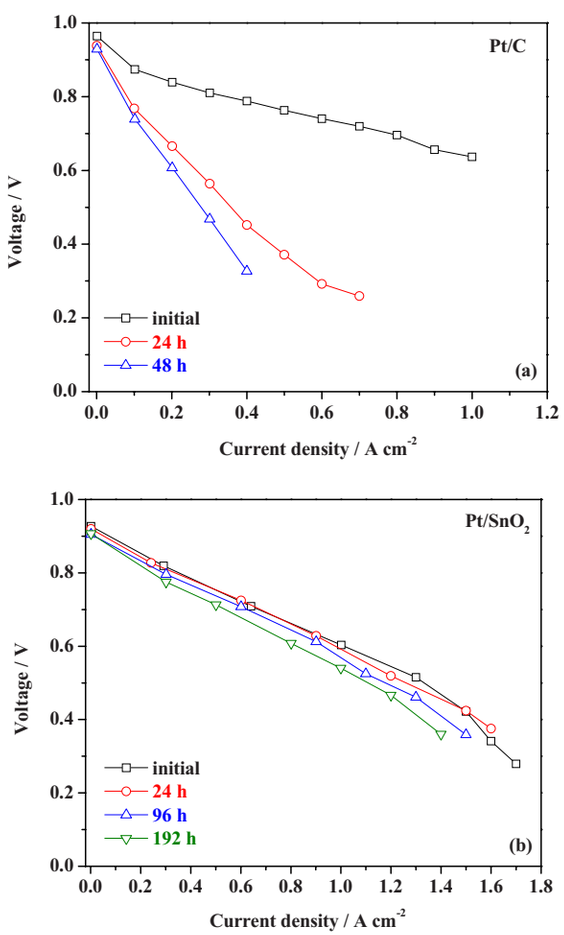

Figure 12. (Color online) Polarization curves for PEMFCs with (a) Pt/C and (b) Pt/SnO_2 catalysts after potential holding tests (ASTP I).

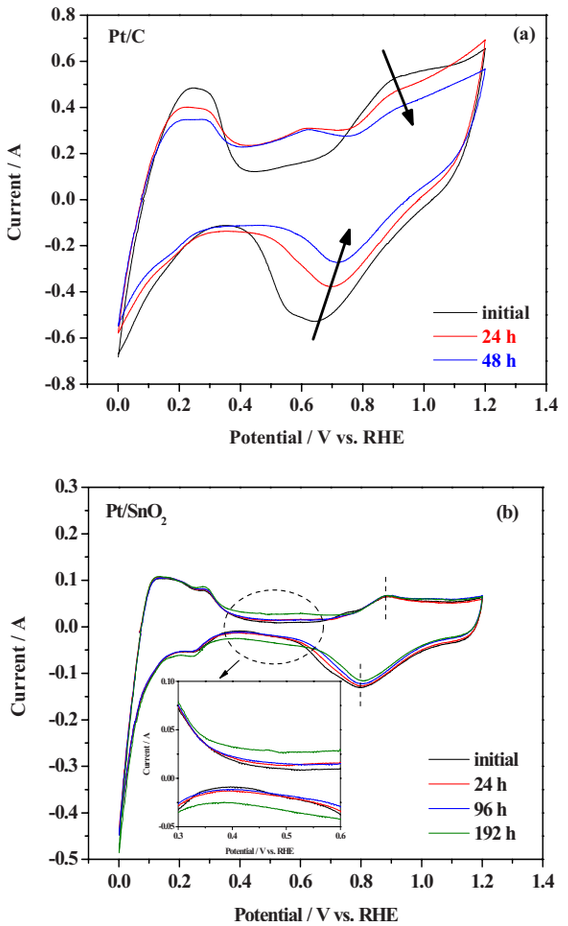

Figure 13. (Color online) CVs of (a) Pt/C and (b) Pt/SnO_2 catalysts after potential holding tests (ASTP I) (inset: CVs in the double-layer region for Pt/SnO_2).

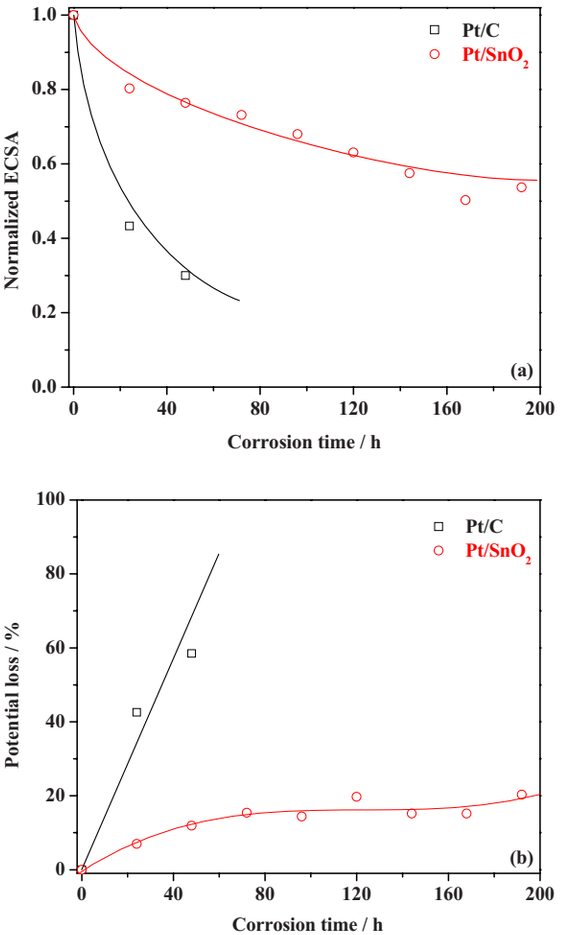

Figure 14. (Color online) (a) Normalized ECSA and (b) potential loss at 0.4 A cm^{-2} as a function of corrosion time for Pt/C and Pt/SnO_2 catalysts.

tained for the Pt/SnO_2 catalyst. Although the average Pt particle size of Pt/SnO_2 (~5.2 nm) was initially larger than that of the Pt/C (~2.5 nm) (shown in Fig. 18), the density of SnO_2 was several folds higher than that of Ketjen Black, resulting in a thin Pt/SnO_2 catalyst layer. Mass transport through this thin catalyst layer was accordingly enforced in Pt/SnO_2, and thus the relatively high fuel cell initial performance was observed.

ASTP I for catalyst support corrosion.— For each MEA, before break-in, the initial fuel cell performance and ECSA were measured, and then potentiostatic scan was held at 1.2 V for 24 h, as described in Table II, before another polarization curve and full-scale CV scan were initiated. The catalyst-support durability is more sensitive to high potentials (>1.2 V) rather than other conditions, and in the mean time potentiostatic scan has little influence on Pt particle sintering. Figure 12 shows polarization curves of the Pt/C and Pt/SnO_2 catalysts before and after potential holding tests (ASTP I). The polarization curve of the Pt/SnO_2 remained nearly unchanged even after a corrosion time of 190 h, while the Pt/C catalyst exhibited a dramatic decrease in fuel cell performance after only 24 h due to severe carbon particle corrosion in the presence of Pt catalysts. The CVs obtained after ASTP I tests are shown in Fig. 13. In this figure, the CVs of Pt/C MEA experienced significant changes. In contrast, the Pt/SnO_2 MEA CVs were much more stable during the whole tests. To carefully compare the properties of both types of catalysts, the ECSA must be normalized because the CV intensity for the Pt/C MEA was much stronger than that for the Pt/SnO_2 MEA. As shown in Fig. 14a, the Pt/SnO_2 catalyst remained ~60% of its initial ECSA even after 190 h, while the ECSA of the Pt/C was reduced by 80% after 48 h as Pt/C peak positions shifted dramatically (indicated by the arrow in Fig. 13).

Furthermore, the potential losses at 0.4 A cm^{-2} as a function of corrosion time for both types of catalysts are compared in Fig. 14b. The Pt/C catalyst suffered a large potential loss with an increase in corrosion time. This is attributed to the thermodynamic instability of carbon supports at high potentials. Additionally, a new peak in the double-layer region (at about 0.6 V) on the Pt/C catalyst was clearly observed (as shown in Fig. 13a), which indicated that additional carbon oxidation occurred.[30] The potential loss in Pt/SnO_2 was barely changed. Neither new peaks in the double-layer region nor characteristic peak position shifts were observed for the Pt/SnO_2 catalyst (as shown in Fig. 13b). Based on the thermodynamic analysis of the Pourbaix diagram of the Sn–H_2O system at 80°C,[33] SnO_2

Table III. ASTP II.

	Electrocatalyst cycle
Cycle	Linear potential sweep from 0.7 to 1.2 V
Number	5000 cycles
Temperature	70, 75, 80, 85, and 90°C
RH	Anode/cathode 100/100%
Fuel/oxidant	Hydrogen/nitrogen
Pressure	150 kPa absolute

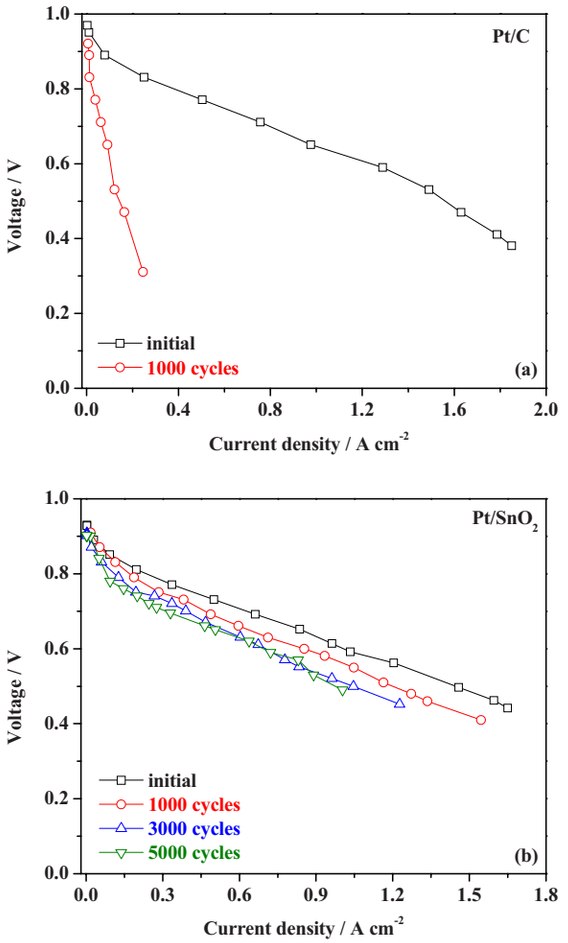

Figure 15. (Color online) Polarization curves for PEMFCs with (a) Pt/C and (b) Pt/SnO_2 catalysts after potential cycling tests (ASTP II) at 80°C.

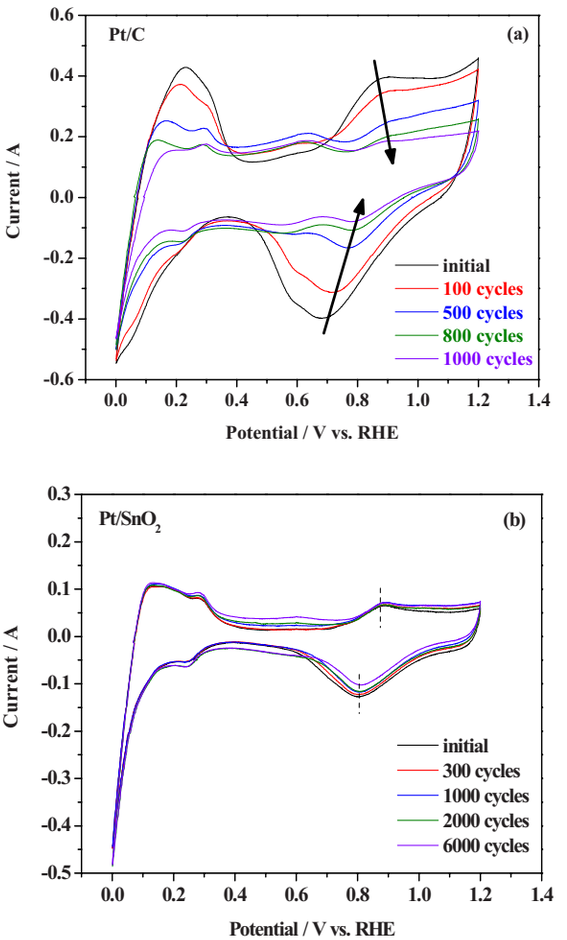

Figure 17. (Color online) CVs of (a) Pt/C and (b) Pt/SnO_2 catalysts after potential cycling tests (ASTP II) at 80°C.

is the most stable compound in the Sn–H_2O system under conditions similar to a typical PEMFC operation. In other words, SnO_2 as a catalyst support is much robust against electro-oxidation at high potentials. SnO_2 as an oxidation-resistant catalyst support is targeted to be used in the unitized regenerative fuel cell (URFC) applications, which operates at very positive potentials (>1.5 V) when URFC is used in the water electrolyzer mode. Medium temperature fuel cells such as phosphoric acid fuel cell can also benefit with SnO_2 support.

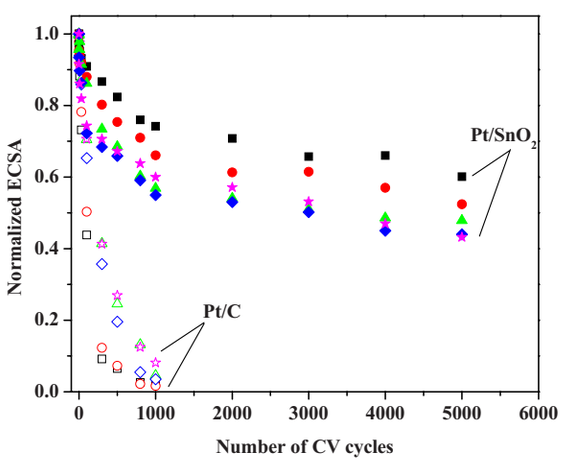

Figure 16. (Color online) Normalized ECSA as a function of CV cycling numbers for the Pt/C and Pt/SnO_2 catalysts at 70°C (square), 75°C (circle), 80°C (triangle), 85°C (star), and 90°C (diamond).

ASTP II for Pt particle sintering.— To investigate the issue of Pt particle sintering in proton exchange membrane MEAs, the potential cycling tests between 0.7 and 1.2 V were applied to the MEAs with Pt/C and Pt/SnO_2 cathode catalysts (as described in Table III). The initial polarization curves and ECSA for both cases were measured before the potential sweeping started. The cycling tests were periodically stopped, and then the current–voltage curves and ECSA were measured. Figure 15 shows the polarization curves of the Pt/C and Pt/SnO_2 before and after potential holding tests (ASTP II) at 80°C. From Fig. 15, the performance loss of the Pt/C catalyst was clearly much more significant than that of the Pt/SnO_2 catalyst after only 1000 cycles. Changes in ECSA, catalyst activity, overall MEA impedance, and mass transport could mainly contribute to this performance loss.[1]

The potential cycling tests were repeated with a new set of MEAs but at different cell temperatures (70, 75, 80, 85, and 90°C). The normalized ECSA vs potential cycling numbers for the Pt/C and Pt/SnO_2 catalysts at all the temperatures are shown in Fig. 16. In the Pt/SnO_2 catalyst, the normalized ECSA stabilized at around 60% for all temperatures after 5000 cycles, while the ECSA of the Pt/C catalyst decreased by more than 90% in the first 1000 cycles. To provide further evidence from potential cycling, the CVs of the Pt/C and

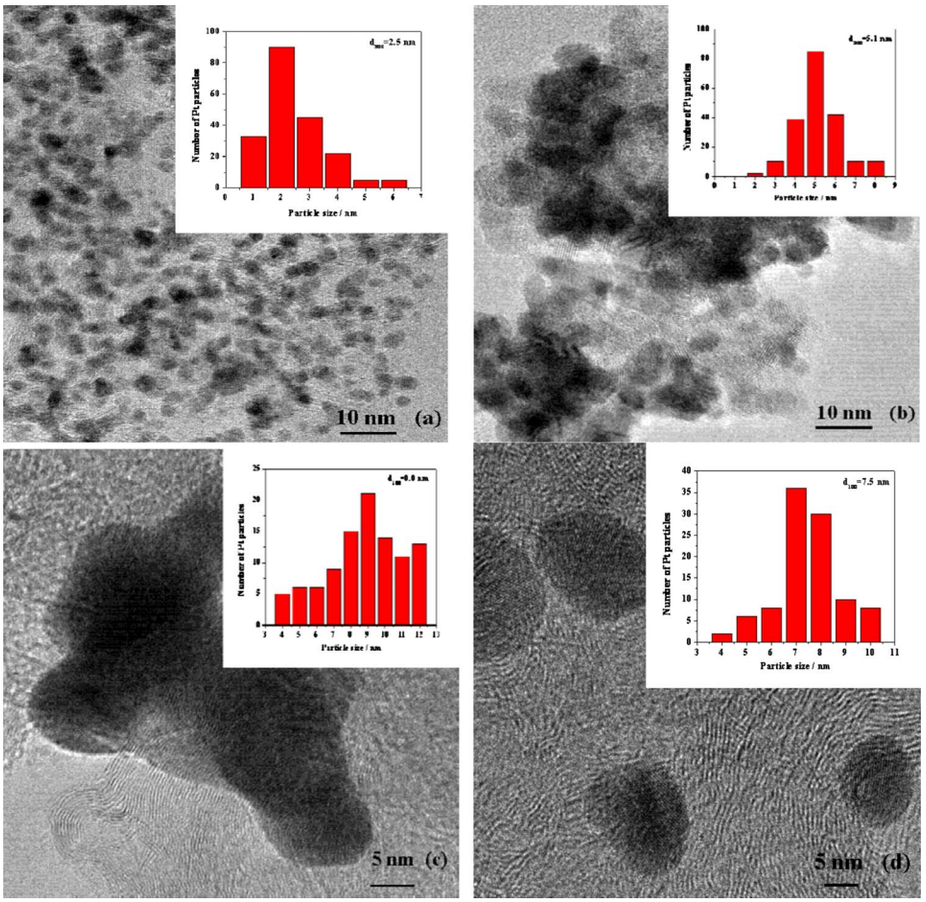

Figure 18. (Color online) TEM images of the Pt/C [(a) initial and (c) after ASTP II at 80°C] and Pt/SnO_2 [(b) initial and (d) after ASTP II at 80°C] catalysts.

Pt/SnO_2 catalysts cycled at 80°C, for example, are shown in Fig. 17. The results indicated that the potential cycling led to proportional drops in such surface-area-dependent processes as electrochemical adsorption and desorption of hydrogen (0–0.4 V), double-layer charging (0.4–0.6 V), and Pt–OH formation and reduction (0.6–1.2 V). The hydrogen adsorption–desorption peaks were poorly defined on Pt/C catalyst after 1000 cycles, finally leading to a continuous decrease in ECSA with an increase in cycling numbers. The Pt–OH reduction peaks shifted to high potentials and decreased in intensity (shown in Fig. 17a). This shift reflects a decrease in the adsorption of the oxygen-containing species on the carbon surfaces, which are believed to lower the ORR activity.[34] Such shift is mainly due to the growth of Pt particle size because electrochemical oxidation of carbon supports causes the agglomeration of Pt catalyst particles, which were initially separated from each other by the supports. This modification of the catalyst properties was more remarkable in the potential cycling tests than in the potential holding experiments.

TEM images of the Pt/C and Pt/SnO_2 catalysts are shown in Fig. 18 to provide further evidence of Pt particle growth and agglomeration. Pt particles on the order of 2–3 nm with a narrow distribution in the pristine MEA cathode with Pt/C catalyst have grown up to ~8.8 nm in the cycled MEA cathode at 80°C. In contrast, Pt particle size (initially ~5.1 nm) has increased only to ~7.5 nm in the MEA cathode during the potential cycling tests at the same temperature. The degree of Pt nanoparticles agglomeration on carbon support is higher than that on SnO_2 support. The anchoring effect on the Pt/SnO_2 catalyst is due to the strong interaction between SnO_2 and Pt metal because SnO_2 support has rough surfaces. Carbon support, on the contrary, has smooth surfaces on which the interaction between carbon and Pt metal is weak. Kamiuchi et al.[35] carefully studied the interaction between Pt and tin oxide in a reoxidation atmosphere. They concluded that the inhibition of Pt migration and agglomeration was attributed to the formation of a Pt–Sn bond. As to the Pt/C catalyst, the Pt particle growth behavior during potential cycling is under control by a combination of Pt dissolution/reprecipitation and Pt particle coalescence because Pt particle size distributions become broader but do not shift completely to larger particle size ranges.[30] For instance, as shown in Fig. 18c, an increased number of larger Pt particles are observed, but in the mean time, a fraction of smaller Pt particles (<5 nm) remains after potential cycling tests though the total particle number decreases. Pt

Table IV. A summary of average Pt particle size before and after ASTP II.

	d_{Pt} (nm)					
	Initial	70°C	75°C	80°C	85°C	90°C
Pt/C	2.5	5.8	7.1	8.8	10.4	12.2
Pt/SnO_2	5.1	6.2	6.9	7.5	8.8	9.5

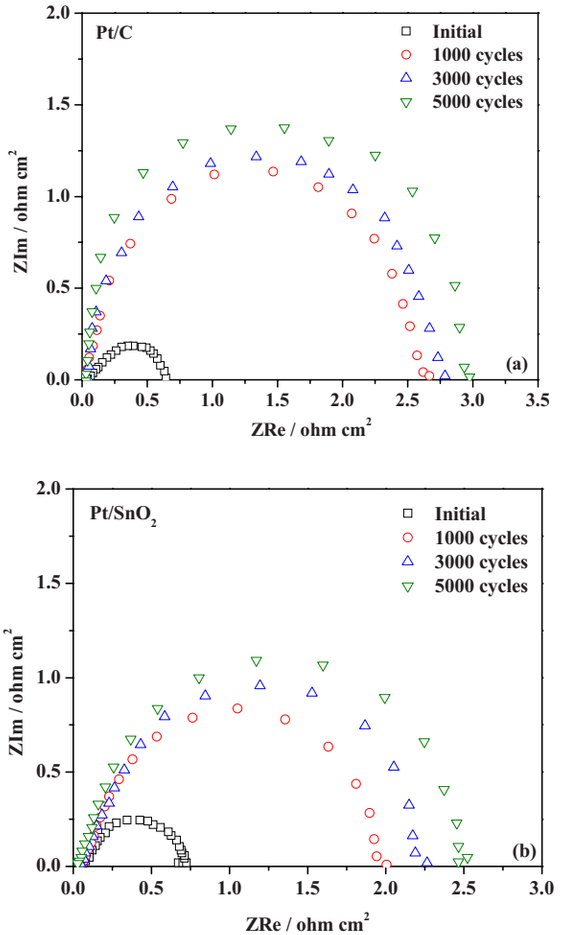

Figure 19. (Color online) Electrochemical impedance spectra for (a) Pt/C and (b) Pt/SnO_2 catalysts collected at 800 mV during ASTP II at 80°C.

coalescence occurs when Pt particles are close to each other and sinter together to form larger particles or clusters.[30] Bi and Fuller[36] developed a simple model to predict the Pt dissolution rates during potential cycling. Taking into account Pt particle size effect, they concluded that the Pt dissolution rates decreased with potential cycling due to the increase in the Pt particle size. Pt particle size distribution shifts to a higher and wider range as a consequence of Pt growth and aggregation after potential cycling tests. Table IV summarizes the average Pt particle size for the Pt/C and Pt/SnO_2 catalysts before and after ASTP II at various temperatures. The average Pt particle size in the Pt/C catalyst increased dramatically with an increase in testing temperatures. Although the average Pt particle size on the Pt/SnO_2 catalyst has also been dependent on operation temperatures, it has still exhibited a narrow distribution (shown in Fig. 18d) and has a much smaller particle size than the Pt/C catalyst.

To investigate the contribution of MEA impedance to the degradation behavior of single cells, electrochemical impedance spectra for the Pt/C and Pt/SnO_2 catalysts were obtained by the ac impedance technique to determine the ohmic (R_{ohm}) and charge-transfer resistances (R_{ct}) of the MEAs before and after potential cycling tests. It has been reported that the cell impedance measured at low overvoltage with pure hydrogen for the anode and high airflow for the cathode is to minimize the anode effect and to lessen the mass-transport effect of the cathode, respectively. Thus, the impedance of the full fuel cell almost equals the cathode impedance due to the fast hydrogen oxidation reaction. In principle, the intersection with the x axis at the high frequency represents the total ohmic resistance, which is the sum of the contributions from contact resistances between components and ohmic resistances of the cell components such as the membrane, catalyst layer, GDL, and bipolar plates.[37] The diameter of the semicircle measures the charge-transfer resistance of the ORR, which is a good indicator of the properties of the cathode such as the catalyst surface area, catalyst loading, and catalyst utilization.[37] As shown in Fig. 19, the standard semicircle appears in all experimental cases. The ohmic resistance (~0.03 Ω cm^2 for Pt/C and ~0.01 Ω cm^2 for Pt/SnO_2) of the MEAs did not significantly change in any case, implying that the membrane resistance was not affected by the potential cycling tests. However, the charge-transfer resistance increased with an increase in cycling numbers, suggesting that the ORR was greatly influenced by the potential cycling tests. The charge-transfer resistance of the Pt/C catalyst increased dramatically from 0.7 to 3.0 Ω cm^2 after 5000 cycles, whereas that of the Pt/SnO_2 catalyst increased slowly (from 0.75 to 2.5 Ω cm^2) over 5000 cycles. In a more specific case, the charge-transfer resistance of the Pt/C catalyst over 1000 cycles was slightly higher than that of the Pt/SnO_2 catalyst after 5000 cycles, indicating that the fuel cell performance of the former was much lower than that of the latter. This was also confirmed by the polarization curves shown in Fig. 15.

Conclusions

In this study, mesostructured SnO_2 nanoparticles with high surface areas were successfully synthesized as a promising cathode catalyst support for PEMFCs. The Pt/SnO_2 catalyst showed good electrochemical activity for ORR and, more importantly, much better stability in CV cycling tests (up to 1.3 V) than the commercial Pt/C catalyst. In addition, to mimic the conditions during the start/shutdown cycle in automotive application, the accelerated stress tests were applied to MEAs with the Pt/C and Pt/SnO_2 catalysts. In ASTP I, SnO_2 sustains a high potential (1.2 V) for almost 200 h with a slight decay, while carbon supports showed a large decrease in surface area due to the electro-oxidation of carbon itself. The durability of the Pt/C and Pt/SnO_2 catalysts was investigated by the potential cycling tests. According to the results from ASTP II, the Pt/SnO_2 catalyst is more stable than Pt/C. The Pt/SnO_2 catalyst approached a maximum of 50% ECSA loss in 5000 cycles, whereas Pt/C lost nearly 90% of the initial ECSA over only 1000 cycles. After potential cycling tests, the Pt/C catalyst showed a dramatic increase in the Pt particle size and a remarkable shift in Pt particle size distribution to a broader range. In contrast, the Pt particle size of the Pt/SnO_2 increased slowly due to the strong interaction between platinum metal and tin oxide.

Acknowledgments

The financial support of NASA-EPSCoR is gratefully acknowledged.

University of South Carolina assisted in meeting the publication costs of this article.

References

1. M. K. Debe, A. K. Schmoeckel, G. D. Vernstrom, and R. Atanasoski, *J. Power Sources*, **161**, 1002 (2006).
2. P. J. Ferreira, G. J. la O', Y. Shao-Horn, D. Morgan, R. Makharia, S. Kocha, and H. A. Gasteiger, *J. Electrochem. Soc.*, **152**, A2256 (2005).
3. K. Yasuda, A. Taniguchi, T. Akita, T. Ioroi, and Z. Siroma, *Phys. Chem. Chem. Phys.*, **8**, 746 (2006).
4. J. F. Wu, X. Z. Yuan, J. J. Martin, H. J. Wang, J. J. Zhang, J. Shen, S. H. Wu, and W. Merida, *J. Power Sources*, **184**, 104 (2008).
5. H. R. Colon-Mercado and B. N. Popov, *J. Power Sources*, **155**, 253 (2006).
6. P. Ferreira-Aparicio, M. A. Folgado, and L. Daza, *J. Power Sources*, **192**, 57 (2009).
7. H. R. Colón-Mercado, H. S. Kim, and B. N. Popov, *Electrochem. Commun.*, **6**, 795 (2004).
8. S. C. Zignani, E. Antolini, and E. R. Gonzalez, *J. Power Sources*, **182**, 83 (2008).
9. C. A. Reiser, L. Bregoli, T. W. Patterson, J. S. Yi, J. D. Yang, M. L. Perry, and T. D. Jarvi, *Electrochem. Solid-State Lett.*, **8**, A273 (2005).
10. K. Kinoshita, *Carbon: Electrochemical and Physicochemical Properties*, p. 319, John Wiley & Sons, New York (1988).
11. L. M. Roen, C. H. Paik, and T. D. Jarvi, *Electrochem. Solid-State Lett.*, **7**, A19 (2004).
12. J. Meyers and R. Darling, Abstract 856, in The 202nd Meeting of the Electrochemi-

cal Society, Salt Lake City, UT, Oct 20–24, 2002.
13. A. Ohma, S. Suga, S. Yamamoto, and K. Shinohara, *ECS Trans.*, **3**(1), 519 (2006).
14. S.F. Burlatsky, V. Atrazhev, N.E. Cipollini, D.A. Condit, and N. Erikhman, *ECS Trans.*, **1**(8), 239 (2006).
15. K. L. More, R. Borup, and K. S. Reeves, *ECS Trans.*, **3**(1), 717 (2006).
16. T. Ioroi, H. Senoh, S. I. Yamazaki, Z. Siroma, N. Fujiwara, and K. Yasuda, *J. Electrochem. Soc.*, **155**, B321 (2008).
17. K. Sasaki, L. Zhang, and R. R. Adzic, *Phys. Chem. Chem. Phys.*, **10**, 159 (2008).
18. K. W. Park and K. S. Seol, *Electrochem. Commun.*, **9**, 2256 (2007).
19. H. Chhina, S. Campbell, and O. Kesler, *J. Power Sources*, **161**, 893 (2006).
20. W. L. Yao, J. Yang, J. L. Wang, and Y. N. Nuli, *Electrochem. Commun.*, **9**, 1029 (2007).
21. K. S. Lee, I. S. Park, Y. H. Cho, D. S. Jung, N. Jung, H. Y. Park, and Y. E. Sung, *J. Catal.*, **258**, 143 (2008).
22. H. Chhina, S. Campbell, and O. Kesler, *J. Electrochem. Soc.*, **154**, B533 (2007).
23. J. Zhu, B. Y. Tay, and J. Ma, *Mater. Lett.*, **60**, 1003 (2006).
24. Z. H. Zhou, W. J. Zhou, S. L. Wang, G. X. Wang, L. H. Jiang, H. Q. Li, G. Q. Sun, and Q. Xin, *Catal. Today*, **93–95**, 523 (2004).
25. V. A. Sethuraman, J. W. Weidner, A. T. Haug, M. Pemberton, and L. V. Protsailo, *Electrochim. Acta*, **54**, 5571 (2009).
26. U.S. DOE, Durability Test Protocol for PEM Fuel Cells (2005).
27. X. Z. Cui, J. L. Shi, H. R. Chen, L. X. Zhang, L. M. Guo, J. H. Gao, and J. B. Li, *J. Phys. Chem. B*, **112**, 12024 (2008).
28. J. X. Wang, N. M. Markovic, and R. R. Adzic, *J. Phys. Chem. B*, **108**, 4127 (2004).
29. X. Li, L. Liu, J. W. Lee, and B. N. Popov, *J. Power Sources*, **182**, 18 (2008).
30. R. Borup, J. Meyers, B. Pivovar, Y. S. Kim, R. Mukundan, N. Garland, D. Myers, M. Wilson, F. Garzon, D. Wood, et al., *Chem. Rev. (Washington, D.C.)*, **107**, 3904 (2007).
31. Y. Y. Shao, G. P. Yin, and Y. Z. Gao, *J. Power Sources*, **171**, 558 (2007).
32. C. Y. Du, M. Chen, X. Y. Cao, G. P. Yin, and P. F. Shi, *Electrochem. Commun.*, **11**, 496 (2009).
33. M. Pourbaix, *Atlas of Electrochemical Equilibria in Aqueous Solutions*, 2nd ed., National Association of Corrosion Engineers, Houston, TX (1974).
34. A. S. Aricò, A. Stassi, E. Modica, R. Ornelas, I. Gatto, E. Passalacqua, and V. Antonucci, *J. Power Sources*, **178**, 525 (2008).
35. N. Kamiuchi, T. Matsui, R. Kikuchi, and K. Eguchi, *J. Phys. Chem. C*, **111**, 16470 (2007).
36. W. Bi and T. F. Fuller, *J. Electrochem. Soc.*, **155**, B215 (2008).
37. X. Z. Yuan, H. J. Wang, J. C. Sun, and J. J. Zhang, *Int. J. Hydrogen Energy*, **32**, 4365 (2007).